

Phase field crystal simulations of the kinetics of Ostwald ripening in two dimensions

Kyle A. Moats,¹ Ebrahim Asadi,² and Mohamed Laradji^{1,*}

¹*Department of Physics and Materials Science, The University of Memphis, Memphis, Tennessee 38152, USA*

²*Department of Mechanical Engineering, The University of Memphis, Memphis, Tennessee 38152, USA*



(Received 25 September 2018; published 22 January 2019)

The kinetics of Ostwald ripening of solid domains in the liquid phase of one-component systems in two dimensions is investigated numerically via the phase field crystal model. The simulations, which are performed systematically as a function of volume fraction of the solid phase, show that dynamical scaling is reached during late times, and the growth law is in good agreement with the classical theory of Lifshitz, Slyozov, and Wagner (LSW), i.e., $\bar{R} \sim t^{1/3}$, an indication that domain growth is mediated by the long-range interdomain diffusion of atoms. In contrast to the LSW theory, however, the domain size distribution is symmetric, and can be fit with a Gaussian. The investigation of the topological domain structure, through the Voronoi tessellation of the domains' centers of mass shows that both the Lewis law and the Aboav–Weaire law of two-dimensional cellular patterns are satisfied, implying that the kinetics proceed such that the conformational entropy of the domain-containing Voronoi cells is maximized. These results are in very good agreement with an earlier experimental study of a phase-separating phospholipid-cholesterol Langmuir film.

DOI: [10.1103/PhysRevE.99.012803](https://doi.org/10.1103/PhysRevE.99.012803)

I. INTRODUCTION

The kinetics of phase separation in materials is crucially important to many materials processes and has thus been the subject of many studies during the last few decades through experiments (see, e.g., Refs. [1–13]), theory see, e.g., Refs. [14–26]), and simulation (see, e.g., Refs. [24,26–34]). Phase separation occurs when a system is rapidly quenched from a homogeneous disordered state to a multiphase region of its phase diagram. The early stages of this process depend on the volume fractions of the coexisting phases. If these volume fractions are comparable, the phase separation is triggered by an instability of the homogeneous concentration against nonlocalized fluctuations with infinitesimal amplitudes, leading to the formation of small domains and their subsequent growth through a process known as spinodal decomposition [35]. However, if the volume fractions of the coexisting phases are very different, such that the initial homogeneous state is supersaturated, the phase separation is triggered by an instability against localized concentration fluctuations with finite amplitudes. This instability leads to the nucleation of the minority phase into small domains and their subsequent growth, to a degree where supersaturation is relieved, through a process known as Ostwald ripening [35,36]. Domain growth in either spinodal decomposition or Ostwald ripening is driven by the minimization of the excess interfacial energy of the domains. In Ostwald ripening, in particular, domain growth proceeds through the long-range evaporation-condensation mechanism, whereby material is transported, through diffusion within the matrix (majority phase), from the shrinking (small) domains to the growing (large) domains.

An interesting feature of the late stages of the kinetics of phase separation is the emergence of a single characteristic length scale with a power-law time dependence, $\bar{R}(t) \sim t^n$, where the growth exponent n indicates the physical mechanism governing the phase separation process. The emergence of a single dominant length scale during the late stages of phase separation implies that structural functions such as the structure factor, correlation function, and domain-size distribution exhibit simple dynamical scaling behavior [35,36]. In alloys, where domain growth proceeds via the evaporation-condensation mechanism, the growth exponent $n = 1/3$. The first theoretical understanding of this growth mechanism was developed by Lifshitz and Slyozov [15] and by Wagner [16]. Although the Lifshitz–Slyozov–Wagner (LSW) theory [15,16] was developed for the case where the volume fraction of the minority phase is infinitesimally small, the growth law predicted by this theory is very robust and is in fact independent of volume fraction, geometry of the domain structure, and spatial dimension. In the case of binary fluids, hydrodynamics play a more important role on their phase separation than the long-range evaporation-condensation mechanism, leading to growth laws that depend on whether domains are connected and on the spatial dimension [35].

The LSW theory [15,16] is based on few ingredients corresponding to a quasistationary approximation of the concentration or density field in the matrix, a boundary condition at the domains interfaces satisfying the Gibbs–Thomson relation, and the requirement of flux conservation at the domains interfaces. The theory predicts an asymptotic average domain size,

$$\bar{R}(t) = [\bar{R}^3(0) + Kt]^{1/3}, \quad (1)$$

where $\bar{R}(0)$ is the initial average domain size in the long-time regime, and K is the coarsening rate. LSW theory also predicts a self-similar behavior, as displayed by the

*mlaradji@memphis.edu

domain-size distribution,

$$g(R, t) \sim G(R/\bar{R}(t))/\bar{R}^{d+1}(t), \quad (2)$$

where G is a time-independent domain-size distribution and d is the spatial dimension. For tractability, the LSW theory was developed for the limit of infinitesimally small volume fractions of the minority phase in three-dimensional systems [15,16]. Extensions of the LSW theory were later made to two-dimensional systems (where the theory suffers from logarithmic singularities), to systems with finite volume fractions [20,21,23–26,28], and to multicomponent systems [37].

Materials properties are usually investigated through microscopic approaches, such as density-functional theory [38] and classical atomistic molecular dynamics [39,40], or mesoscopic approaches, such as phase field models [41]. The phase field crystal (PFC) model is a relatively new phenomenological approach, developed by Elder and Grant [42], which can be derived from classical density-functional theory and leads to a periodic field with atomic-scale structure. The advantage of this model is that, while it accounts for atomic-scale elastic and plastic effects, it is able to describe structural properties on diffusive timescales. The PFC approach has thus been used extensively during the last few years in a range of studies addressing generic phenomena in one-component and two-component materials, including grain boundaries [42], epitaxial growth [43,44], crystallization [45–49], and phase separation kinetics [49,50]. In this article, we present a computational study of the kinetics of Ostwald ripening, of crystalline domains in a liquid matrix of one-component systems in two dimensions, based on the PFC model.

Many experiments have been performed to test the validity of the LSW theory [2,8,11–13,51,52]. Few experiments have also been performed to investigate Ostwald ripening in two-dimensional systems [7,8]. While experiments have shown that domain growth is in accord with Eq. (1), the domain-size distributions from these experiments are broader and more symmetric than predicted by the LSW theory [53].

Numerical simulations of Ostwald ripening in two dimensions through phase field simulations of Model B [30,54] predict a correct growth law ($n = 1/3$). However, the domain-size distributions from these simulations are also broader and more symmetric than predicted by generalized LSW theory in two dimensions [23,54]. Phase field simulations, however, are too coarse grained and do not take into account microscopic details of the systems. Simulations of Ostwald ripening through atomistic molecular dynamics are impractical since the phenomenon occurs on diffusive timescales. We therefore alternatively investigate the feasibility of using the PFC model to examine Ostwald ripening in two dimensions. In agreement with the LSW theory, we observed dynamical scaling during late times with an average domain size that grows as $t^{1/3}$ as a result of the long-range evaporation-condensation mechanism. In contrast to the LSW theory, however, the average domain-size distribution is fairly symmetric and can be fit with a Gaussian, in agreement with Seul *et al.*'s experimental investigation of phase separation of a Langmuir film phospholipid-cholesterol mixture [8]. Using Voronoi tessellation, we also investigated the topological domain structure and found that the distribution of coordination number is symmetric and that the average area of a domain scales linearly

with the number of nearest-neighbor domains, in accord with Lewis' law [55]. We also verified that the coordination number of a domain is correlated with the average coordination number of its neighboring domains through the universally observed Aboav–Weaire law of cellular patterns [55]. We also found strong anticorrelation in nearest-neighbor-domain areas; namely, a growing large domain is on average surrounded by shrinking small domains, and vice versa.

II. MODEL AND NUMERICAL APPROACH

The starting equation describing the kinetics of the dimensionless local density field, $\psi(\vec{r}, t)$, is the conserved Langevin equation [42],

$$\frac{\partial \psi}{\partial t} = \nabla^2 \frac{\delta \mathcal{F}}{\delta \psi} + \zeta, \quad (3)$$

where t and \vec{r} are reduced time and space, and ζ is a reduced Gaussian noise with zero mean and a temporal-spatial correlation,

$$\langle \zeta(\vec{r}, t) \zeta(\vec{r}', t') \rangle = \mathcal{D} \nabla^2 \delta(\vec{r} - \vec{r}') \delta(t - t'). \quad (4)$$

The PFC approach is based on a free-energy functional given by

$$F(\{\psi\}) = \int d\mathbf{r} \left\{ \frac{\psi}{2} [\beta + (1 + \nabla^2)^2] \psi + \frac{\psi^4}{4} \right\}, \quad (5)$$

where β is an effective reduced temperature. Using the free-energy functional above, Eq. (3) then becomes

$$\frac{\partial \psi}{\partial t} = \nabla^2 [\beta + (1 + \nabla^2)^2] \psi + \zeta. \quad (6)$$

Here, since we are interested in the late stages of phase separation where thermal fluctuations are not as important as during the early stage of nucleation, the thermal noise is set to zero, i.e., $\zeta(\vec{r}, t) = 0$. Equation (6) is integrated numerically by using a semi-implicit spectral method according to the following algorithm [42]:

(1) Setup of an initial inhomogeneous configuration of $\psi(\vec{r}, t = 0)$ with an average value ψ_0 , beyond the early stages nucleation regime, such that there are $N(0)$ circular solid domains, with a local average density ψ_S in a liquid background of density ψ_L . The average size of the solid domains is $\bar{R}(0)$. The domains' centers of mass are distributed randomly, with a size distribution predicted by Ardell [23].

(2) Calculations of the Fourier transforms $\tilde{\psi}(\vec{k}, t)$ and $\tilde{\psi}^3(\vec{k}, t)$ of $\psi(\vec{r}, t)$ and $\psi^3(\vec{r}, t)$, respectively.

(3) $\psi(\vec{k}, t + \Delta t)$ is calculated by using the approximation [56]

$$\tilde{\psi}(\vec{k}, t + \Delta t) = e^{\omega(k)\Delta t} \tilde{\psi}(\vec{k}, t) - \frac{k^2}{\omega(k)} [e^{\omega(k)\Delta t} - 1] \tilde{\psi}_3(\vec{k}, t), \quad (7)$$

where the amplification factor

$$\omega(k) = -k^2 [\beta + (1 - k^2)^2]. \quad (8)$$

(4) Calculation of the inverse Fourier transform $\psi(\vec{r}, t + \Delta t)$, and repeat steps 2–4.

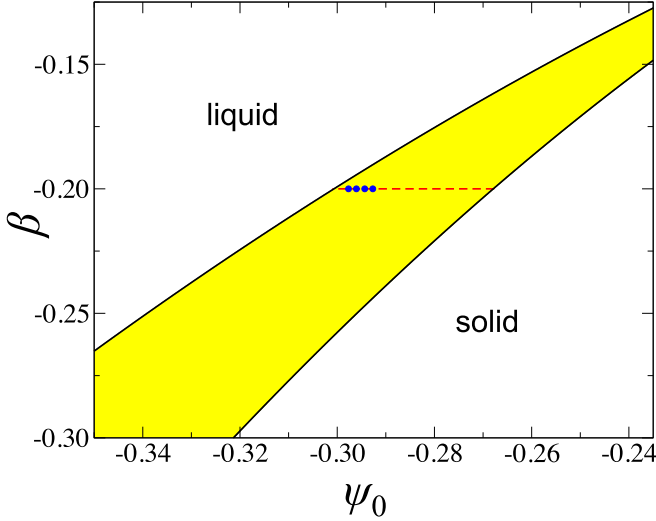


FIG. 1. Portion of interest of the phase diagram of the PFC model in two dimensions. The region of coexistence between the crystalline solid and liquid phases is shown in yellow. The solid lines on the left and right correspond to the solidus and liquidus lines, respectively, and are obtained from numerical solutions of Eq. (6). Isolated points from right to left correspond to area fraction of the solid phase with $\sigma = 0.1, 0.15, 0.2$, and 0.25 , respectively.

The numerical integration was performed by using a CUDA code developed by us. The Fourier transforms were calculated by using the freely available CUFFT distributed-memory parallel code on a square grid of mesh size $\Delta x = \pi/4$. We used an integration time step $\Delta t = 2.0$ in reduced units. In two dimensions, the model predicts a stripe phase and physically relevant triangular and homogeneous (liquid) phases. The simulations were performed at the effective temperature $\beta = -0.2$ in the liquid-solid coexistence region of the phase diagram, partially shown in Fig. 1, and for $-0.29767 \leq \psi_0 \leq -0.29268$. These systems correspond to $\psi_L = -0.3010$ at the liquidus line and $\psi_S = -0.2677$ at the solidus line. The area fraction of the solid phase, $\sigma = (\psi_L - \psi_0)/(\psi_L - \psi_S)$, the initial average domain size, and the initial number of domains of the systems considered in this study are shown in Table I. All simulations are performed on systems with lateral size $L = 6433.98$ and four independent runs were performed on each system.

III. RESULTS

Domain growth is illustrated by a time-sequence of snapshots shown in Fig. 2 for the case of $\sigma = 0.25$. This figure

TABLE I. Average density ψ_0 and corresponding area fraction of the solid phase, σ , initial average domain size $\bar{R}(0)$, and initial number of domains, $N(0)$, of the systems simulated at $\beta = -0.2$.

ψ_0	σ	$\bar{R}(0)$	$N(0)$
-0.29767	0.10	49.14	31
-0.29605	0.15	47.74	50
-0.29434	0.20	47.74	67
-0.29268	0.25	45.88	88

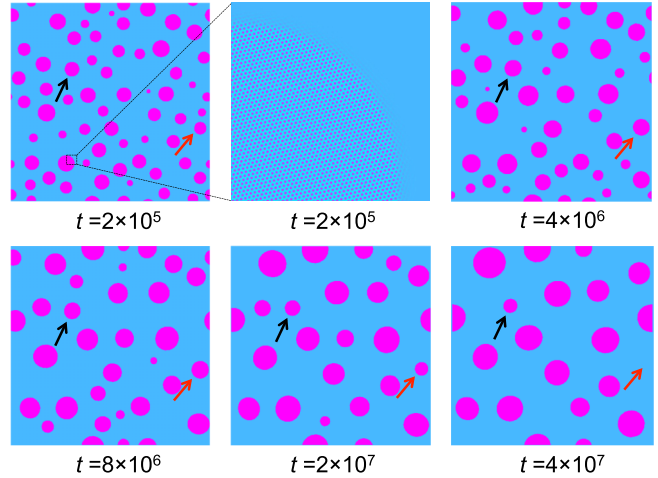


FIG. 2. Time sequence of snapshots for a the case of $\sigma = 0.25$ and $\beta = -0.2$. The black and red arrows point to two domains that grew and then decayed at later times. The domain indicated by the red arrow disappears by $t = 4 \times 10^7$.

demonstrates that, on average, domains coarsen with time, but not as a result of their coalescence. Domains must therefore coarsen via Ostwald ripening, i.e., the evaporation of atoms from shrinking domains and their condensation on growing domains. Figure 2 also shows, as expected during Ostwald ripening, that domains grow and then decay as a function of time (e.g., domains pointed to by the black and red arrows in Fig. 2). Furthermore, Fig. 2 also shows that the domains are only slightly distorted from a circular shape.

The average domain size, calculated as

$$\bar{R}(t) = \frac{1}{N(t)} \sum_{i=1}^{N(t)} R_i, \tag{9}$$

where $N(t)$ is the number of domains at time t , is shown in Fig. 3(a) for all considered values of σ . This figure demonstrates that domain coarsening is in line with LSW theory, i.e., $\bar{R}(t) \sim t^{1/3}$ [Eq. (1)], with a coarsening rate that increases with increasing area fraction of the solid phase, in agreement with previous theories of Ostwald ripening in two dimensions [20,23,24]. An interesting feature, shown by Fig. 3(a), is that, although, on average, $\bar{R}(t)$ increases with time, this increase is not monotonic. Instead, $\bar{R}(t)$ increases in steps with the average domain size that in fact anomalously decreases with time during each step. We show later that this behavior is due to the small number of domains in the system and to the fact that the material evaporating from the shrinking domains does not instantaneously condense on the growing domains. Each discontinuity in $\bar{R}(t)$ corresponds to a single event of domain disappearance. Figure 3(a) also shows that, on average, the timescale of each tread in \bar{R} vs t decreases with increasing σ . This is simply due to the fact that the number of domains increases with increasing σ , and therefore the number of domains disappearance events increases with increasing σ .

Figure 3(b) confirms that, on average, the net area of the coarsening crystalline domains, $N(t)\bar{R}^2(t)$, is indeed conserved, as expected, and that the net area of the solid domains is proportional to the area fraction of the solid phase [see inset

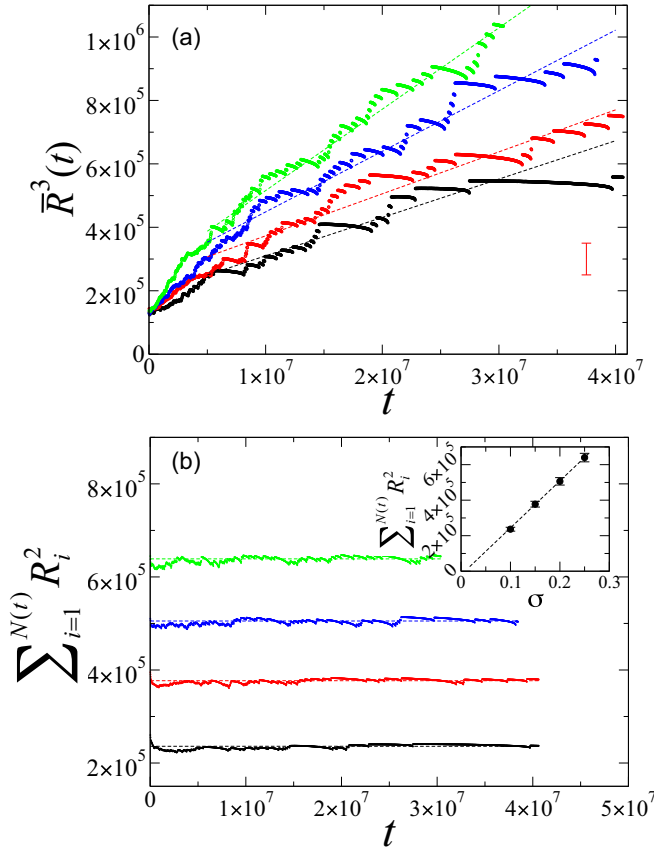


FIG. 3. (a) $\bar{R}^3(t)$ size versus t for $\beta = -0.2$. Black, red, blue, and green points correspond to $\sigma = 0.1, 0.15, 0.2$, and 0.25 , respectively. The dashed lines are linear fits of the numerical data. The maximum error bar of the data is shown in the bottom left of panel (a). (b) The net area of the solid phase $\sum_{i=1}^{N(t)} R_i^2(t)$ vs time for the systems shown in panel (a). The same colors as in panel (a) are used. The dashed lines are horizontal. The inset shows that the average value of $\sum_{i=1}^{N(t)} R_i^2(t)$ is indeed proportional to the area fraction of the solid phase.

of Fig. 3(b)]. However, the net area of the domains is not instantaneously conserved. The small amplitude fluctuations in the net area of the solid phase are correlated with the discontinuities in $\bar{R}(t)$ vs time shown in Fig. 3(a).

In this article, we are interested in the case where domains are rounded. As previously noted, the advantage of the PFC approach, in contrast to the phase field approach, is that it accounts for the crystallinity of the solid phase. We therefore also performed a few simulations for lower values of β and found that the domains are faceted for $\beta < -0.25$, as shown by the snapshots in Fig. 4 for the case of $\beta = -0.30$. During intermediate times, domains grow in accord with Lifshitz–Slyozov theory, as shown by the graph of Fig. 4. However, we found that domain growth anomalously slows down and halts at late times, in contrast with the case where domains are rounded. We repeated the simulations for smaller mesh sizes and time steps and found the same results. The observed slowing down at late times may be attributed to the fact that, at late times, the local curvature of a faceted domain becomes independent of the domain size, R . This is due to the fact that the local curvature of the straight edges is zero, while the local

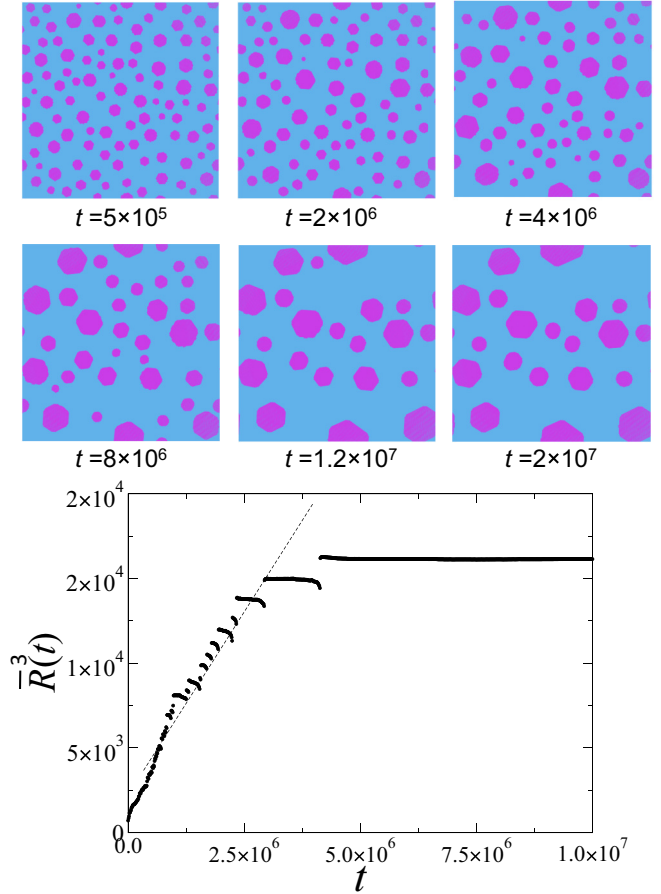


FIG. 4. Time sequence of snapshots for the case of $\beta = -0.30$ and $\sigma = -0.25$ (corresponding to $\psi_0 = -0.37816$). The bottom graph shows $\bar{R}^3(t)$ vs time.

curvature of the vertices is a function of the crystallinity and is independent of the domain size.

We now turn to the discontinuous growth in $\bar{R}(t)$, shown in Fig. 3(a), we performed a simulation of a system consisting of one small domain of initial radius $R_{\downarrow}(0) = 100.5$ and two large domains of initial radius $R_{\uparrow}(0) = 201.0$ at $\beta = -0.20$. The centers of mass of the domains are separated by a distance 1020 in dimensionless units. The configuration is such that the centers of mass of the three domains are colinear. We note that we repeated these simulations with different configurations and found similar results. The time dependence of the profile of the ψ field (averaged over small length scales in order to integrate out the short-length-scale oscillations in the solid phase) along the axis containing the domains' centers of mass is shown in Fig. 5. This figure shows that, while the small domain (in the center) shrinks, the density profile of the large domains varies very weakly during this stage. Figure 6(a), where the average sizes of the shrinking domain (red curve) and growing domains (green curve) vs time are shown, demonstrates that the shrinking and growing domains sizes do not vary simultaneously: While the small domain shrinks, the large domains are not growing, implying that the material evaporating from the shrinking domain is contributing to the increase in the density of the liquid around the shrinking domain, as shown by Fig. 6(d). This is due to the

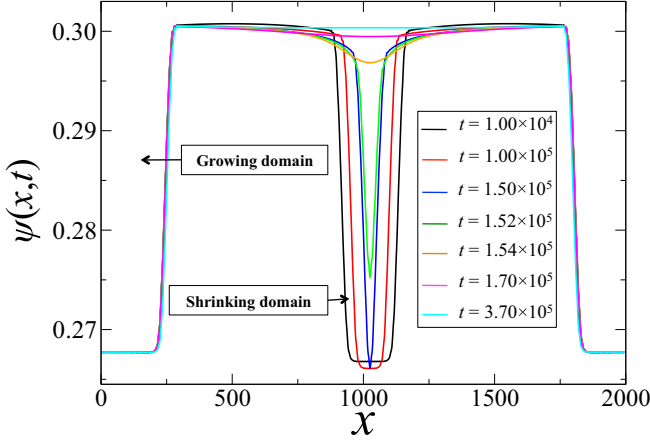


FIG. 5. Evolution of the density profile of a simulation composed of a small and large domain at $\beta = -0.20$. The density profile is averaged over short length scales to integrate out the atomic-scale oscillations in the solid phase.

fact that material evaporation is faster than material diffusion during this process. It is worthwhile noting that Fig. 6(b) shows that the decay rate of the shrinking domain agrees with LSW's growth rate equation

$$\frac{dR(t)}{dt} = \frac{D}{R(t)} \left(\frac{l}{R_c(t)} - \frac{l}{R(t)} \right), \quad (10)$$

where D is the material diffusion constant and $R_c(t)$ is the time-dependent critical radius. The average domain size of this system, shown in Fig. 6(c), has the same features as that of

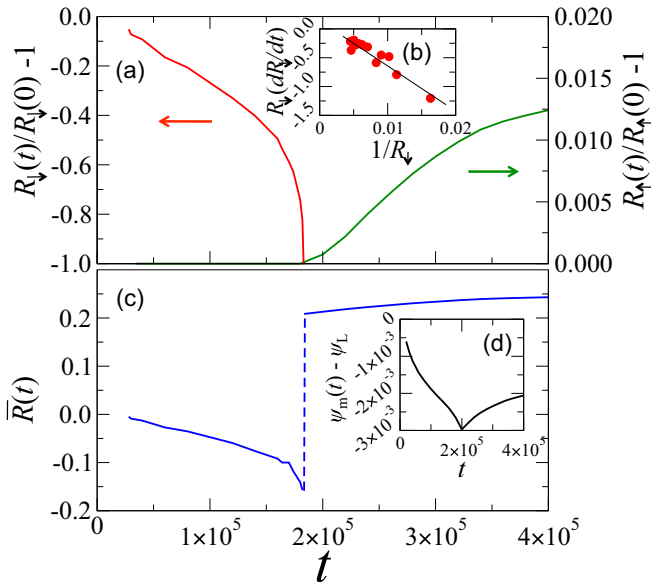


FIG. 6. (a) Red curve shows the radius of the shrinking domain, normalized by its initial value, $R_d(t)/R_d(0) - 1$ vs time. Green curve shows the average radius of the growing domains, normalized by their initial value, $R_g(t)/R_g(0) - 1$ vs time. Inset (b) shows the linear relationship between $R_d(dR_d/dt)$ and $1/R_d$, in accord with Eq. (10). (c) The average domain size vs time. Inset (d) shows the deviation of the ψ field in the region within the liquid phase between the shrinking domain and the growing domains.

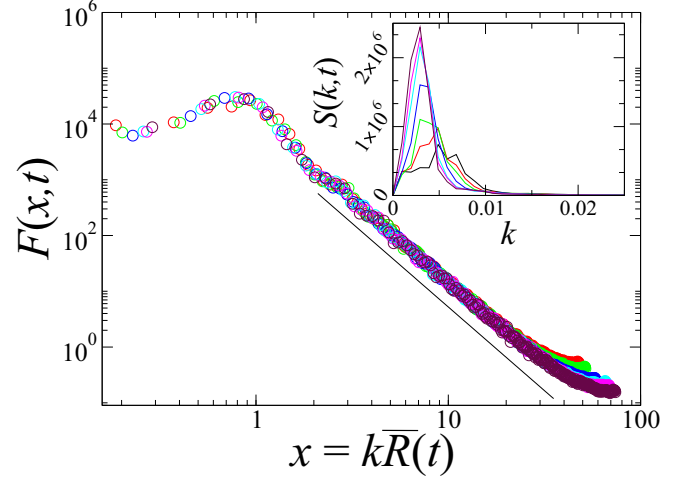


FIG. 7. Scaled structure factor, $F(x, t) = S(k, t)/\bar{R}^2(t)$, where the scaled wave vector $x = k\bar{R}(t)$ for the case of $\sigma = 0.20$ and $\beta = -0.2$. Data shown correspond to 1.2×10^5 (black), 1.32×10^6 (red), 2.52×10^6 (green), 7.32×10^6 (blue), 1.45×10^7 (cyan), 2.18×10^7 (magenta), 3.86×10^7 (maroon) vs k . Inset shows the time evolution of the structure factor, $S(k, t)$ vs k . Times shown are 1.20×10^5 (black), 1.32×10^6 (red), 2.52×10^6 (green), 7.32×10^6 (blue), 1.45×10^7 (cyan), 2.18×10^7 (magenta), and 3.86×10^7 (maroon). The slope of the solid line in the main graph is three, showing that Porod's law is satisfied.

Fig. 3(a); namely, a discontinuity occurring at the time where a shrinking domain disappears, and a decay of the average domain size right before the discontinuity.

As stated earlier, the late-time kinetics of phase separation is marked by the presence of a single characteristic length scale, which implies that structural functions such as the structure factor should exhibit a dynamical scaling behavior,

$$S(k, t) = \langle |\tilde{\psi}(\vec{k}, t)|^2 \rangle = \bar{R}^d(t) F(x), \quad (11)$$

where $x = k\bar{R}(t)$ is the scaled wave vector, $\tilde{\psi}$ is the Fourier transform of ψ , and $F(x)$ is the time-independent scaling function. The presence of a small wave vector peak in $S(k, t)$, shown in the inset of Fig. 7, implies that the domains are spatially correlated, as expected during Ostwald ripening and spinodal decomposition. The time independence of the scaling function, $F(x)$, shown in Fig. 7 (which begins at about 11.0×10^6), implies that the kinetics of Ostwald ripening in the present study is indeed in the scaling regime. The presence of a single length scale during late times implies that other shorter length scales in the system, particularly the thickness of the domains interfaces, should be very small in comparison with the average domain size. Scattering from well-defined domain interfaces should therefore obey Porod's law at large wave vectors, $S(k) \sim k^{-(d+1)}$ [57]. The scaled structure factor, shown in Fig. 7 does indeed scale as x^{-3} for large wave vectors, further confirming that dynamical scaling is indeed reached in the simulations.

The normalized scaled domain size distribution $G(z)$, where $z = R/\bar{R}(t)$ [Eq. (2)] is shown in Fig. 8 for all considered values of σ . We found that, during late times, $G(z)$ is time independent, implying again that the systems are in the dynamical scaling regime, in agreement with Fig. 8.

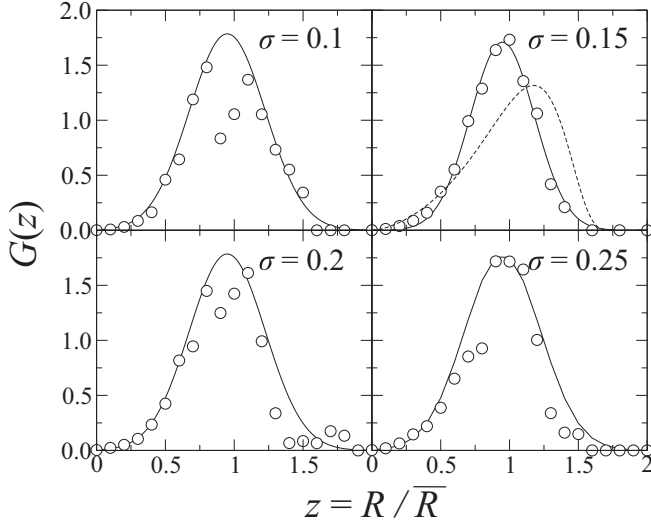


FIG. 8. Normalized scaled domain distribution $G(R/\bar{R})$ vs R/\bar{R} at $\beta = -0.20$. The solid lines are fits with Gaussians. The dotted line in the case of $\sigma = 0.15$ corresponds to Ardell's generalized Lifshitz–Slyozov prediction for the same area fraction in two dimensions [23].

This figure shows that the domain-size distributions for all values of σ are fairly symmetric and can be well fit by a Gaussian, in contrast with the theoretically predicted mean-field distribution by Ardell in two dimensions, shown by the dashed curve for the case of $\sigma = 0.15$ [23]. Our results are in very good agreement with an earlier experiment of Ostwald ripening of a two-component Langmuir surfactant monolayer at an air-water interface [8] and numerical solution of the Cahn–Hilliard equation [54]. The standard deviation of the Gaussian fits of the distributions in Fig. 8 ranges between 0.21 for $\sigma = 0.25$ and 0.3 for $\sigma = 0.1$. These values are close to those obtained by Seul *et al.*, which are about 0.22 [8].

We also characterized the topological domain structure during Ostwald ripening, as predicted by the PFC model in two dimensions, through the Voronoi tessellation based on the domains' centers of mass. For illustration, Fig. 9 shows a snapshot of the domains with links to their nearest-neighbor domains, as obtained from the Voronoi tessellation. The coordination number probability of the domains, $P(q) = N(q)/N$, is shown in Fig. 10(a) for the case of $\sigma = 0.25$, where $N(q)$ is the number of domains with q nearest-neighbor domains and $N = \sum_q N(q)$. $P(q)$ is symmetric and centered at $q = 6$. We found that $P(q)$ quickly becomes time independent and is independent of σ . The values of $P(q) \neq 0$ for $q > 6$ or $q < 6$ implies that the domain structure is characterized by a large amount of topological defects. Interestingly, the values of $P(q)$ are in very good agreement with the experimental values obtained by Seul *et al.* [8]. The second moment of $P(q)$, $\mu_2 = \sum_q (q - 6)^2 P(q) \approx 0.8$, which is also very close to the values reported by Seul *et al.* [8].

We also found a linear relation between the average area of q -coordinated domains, normalized by the average domain area, $\bar{A}(q)/\bar{A}$, with the topological charge $Q = q - 6$, as shown in Fig. 10(b). This result is in accord with Lewis' law of cellular patterns [55],

$$\frac{\bar{A}(q)}{\bar{A}} = \alpha + \gamma Q, \quad (12)$$

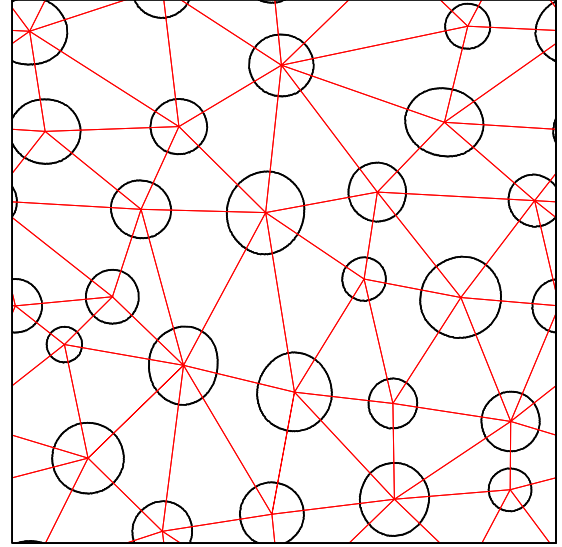


FIG. 9. Snapshot of the domains (perimeters shown in black) with links (red lines) to their nearest-neighbor domains, as obtained from the Voronoi tessellation. Data shown correspond to the case of $\sigma = 0.25$ and $\beta = -0.20$.

universally observed in many systems such as two-dimensional foam [58], epithelial cells [59], and stratocumulus clouds [60]. Equation (12) implies that domains with a coordination number $q = 6$ tend to have a size equal to the average domain size in the system, and that domains that are larger (smaller) than the average domain size tend to have a coordination number larger (smaller) than six. This result indicates that domains are positioned such that the configurational entropy is maximized [59]. We found that the coefficients, in Eq. (12), $\alpha \approx 1.0$ and $\gamma \approx 0.23$ for the case of $\sigma = 0.25$,

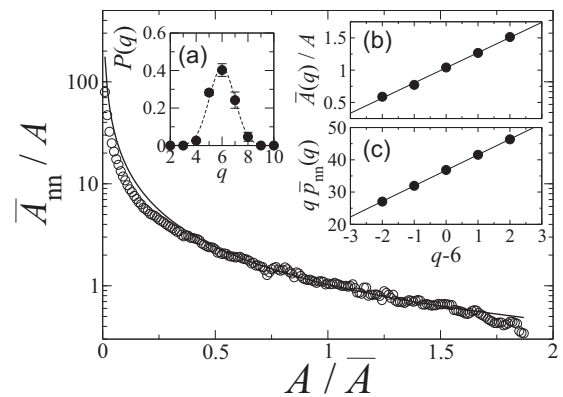


FIG. 10. Normalized average area of nearest-neighbor domains, \bar{A}_{nn}/\bar{A} vs A/\bar{A} for the case of $\sigma = 0.25$ and $\beta = -0.20$. The solid line is from Eq. (14) with parameters γ and b obtained from fits with Eqs. (12) and (13), respectively. Inset (a) shows the coordination number probability $P(q)$ vs q for the case of $\sigma = 0.25$. The dashed line is simply a guide to the eye. Inset (b) shows $\bar{A}(q)/\bar{A}$ vs topological charge, in agreement with Lewis' law (12). Inset (c) shows the average coordination number of nearest-neighbor domains of q -coordinated domains vs topological charge, in agreement with the Abaov–Weaire law (13).

again in good agreement with Seul *et al.*'s results [8]. It is important to note that Lewis' law applies to the areas of the Voronoi cells, while we verified this law by using the domains areas. Dynamical scaling, however, implies that the average distance between neighboring domains is proportional to the average domain size. Hence, Eq. (12) should apply to the domains areas as well.

Optimal space filling of cellular patterns also requires another universally observed topological correlation between the coordination number of a domain, q , with the average coordination number of its nearest-neighbor domains, $\bar{p}_{nn}(q)$, known as the Aboav–Weaire law [55,61],

$$q\bar{p}_{nn}(q) = (6 - b)(q - 6) + c, \quad (13)$$

with $c = 36 + \mu_2$. This relation states that domains with high (low) coordination number, i.e., large (small) domains according to Lewis' law [Fig. 10(b)] are surrounded by small (large) domains. Figure 10(c) shows that the Aboav–Weaire law is indeed satisfied during the kinetics of Ostwald ripening through the PFC model, with $b \approx 1.18$ and $c = 36.75 \approx 36 + \mu_2$, by using the earlier above-found value of $\mu_2 \approx 0.8$. We note that these results are again in very good agreement with Seul *et al.*'s findings [8].

We also inferred the correlation between the area of a domain, A , and the average area of its nearest-neighbor domains,

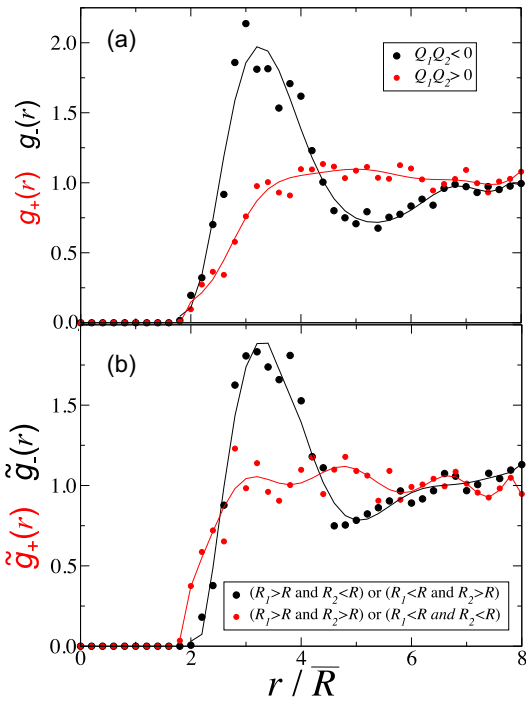


FIG. 11. (a) Charge-charge radial correlation function. Black circles show correlation function between domains with opposite charge signs. Red circles show correlation function between domains with same charge signs. (b) Radial domains size-size correlation. Black circles show correlation function between two domains with one having a size larger than the average domain size \bar{R} , and the other one with a radius smaller than \bar{R} . Red circles show radial correlation between two domains where both are either larger or smaller than \bar{R} . Data shown in insets (a) and (b) are for the case of $\sigma = 0.25$ and $\beta = 0.20$.

\bar{A}_{nn} . Figure 10 shows that \bar{A}_{nn}/A and A are anticorrelated. Namely, domains larger (smaller) than the average domain size are mostly surrounded by nearest-neighbor domains that are smaller (larger) in size. Using a maximum entropy theory for random two-dimensional cellular patterns, Sire and Seul [62] showed that the relationship between $x = A/\bar{A}$ and $f(x) = \bar{A}_{nn}/A$ is given by

$$f(x) = \frac{1}{x} \left[1 + \frac{\gamma^2 \mu_2 - b\gamma(x-1)}{6\gamma + (x-1)} \right]. \quad (14)$$

Figure 10 shows that \bar{A}_{nn}/A and A/\bar{A} are indeed anticorrelated, and that Eq. (14) is indeed satisfied.

The correlations above can also be inferred through two-point correlation functions as a function of distance between domains' centers of mass. The two-point charge-charge correlation functions, $g_+(r)$ and $g_-(r)$, are defined as the correlation functions between two domains with $Q_1 Q_2 > 0$ and $Q_1 Q_2 < 0$, respectively. Figure 11(a) shows that domains with topological charges of opposite signs are much more correlated at short distances (black curve) than domains with either both positive or negative topological charges (red curve). This is another qualitative confirmation of the Aboav–Weaire law; Fig. 10(c). Likewise, Fig. 11(b) shows that domains with a size larger (smaller) than the average domain size are also correlated within short distances with domains with size smaller (larger) than the average domain size, in accordance with the main graph of Fig. 10.

IV. SUMMARY AND CONCLUSION

In this article, we presented an investigation of the kinetics of Ostwald ripening of solid domains in a liquid matrix of one-component systems in two dimensions from a numerical simulation of the single mode PFC model of Elder and Grant [42]. We found that the average domain size $\bar{R}(t)$ grows with time as $t^{1/3}$, in agreement with experiments [7,8], prior simulations using the Cahn–Hilliard equation [54], and LSW theory [15,16]. These results therefore further confirm the validity of the LSW theory and, in particular, that the details of the atomic-scale crystalline structure do not affect the kinetics during late times in the case where the domains are rounded. For low temperatures ($\beta < -0.25$), domains are faceted, and their growth agrees well with the LSW theory at intermediate times. At later times, however, the dynamics is slowed down leading to very slow or halted kinetics.

The domain-size distribution is found to be symmetric and is well fit by a Gaussian, in disagreement with Lifshitz–Slyozov–Wagner theory [23] which predicts a highly non-symmetric distribution. The domain-size distribution from the present simulations is, however, in very good agreement with the earlier experimental study by Seul *et al.* [8] of the kinetics of Ostwald ripening of a binary phospholipid-cholesterol Langmuir film. We also confirmed that the systems reached dynamical scaling during late times, as demonstrated by scaling of the density structure factor.

Our investigation of the topological structure of the two-dimensional system during Ostwald ripening, inferred from the Voronoi analysis, indicates that the domains are positioned in space so as to maximize the configurational entropy of

the domains' centers of mass. In particular, we showed that the average size of the q -coordinated domains follows Lewis' law, i.e., domains with high coordination number are larger than the average domain size, and vice versa. Furthermore, the average coordination number of neighboring domains of a given q -coordinate number follows the Aboav–Weaire law, i.e., domains with high coordination numbers are surrounded, on average, by domains with low coordination numbers. In other words, the system adopts a structure such that deviations from a neutral topological charge is minimized. Our results on the topological structure of the coarsening system are in very good agreements with earlier experimental results of Seul *et al.* [8,62].

The present study represents a detailed test of Ostwald ripening kinetics in two-dimensional one-component systems through the PFC approach. Successful attempts have been made to generalize the PFC approach to one-component systems with various crystalline structures through the addition of higher-order gradients of the density field [63]. The PFC

approach also has the capability to quantitatively describe specific materials with various crystalline structures [64]. With further generalizations of PFC to multicomponent systems through coupling the density field to the composition field [45], future numerical investigations using PFC of Ostwald ripening in specific alloys can be performed on diffusive timescales and quantitatively compared with available experiments.

ACKNOWLEDGMENTS

This work is supported by the National Aeronautics and Space Administration under Grant No. NNX16AT77G issued through the NASA/Marshall Space Flight Center. We also acknowledge the financial support from the FedEx Institute of Technology, Biologistics Research Cluster at the University of Memphis. All simulations were performed on computers of the High Performance Computing facility at the University of Memphis.

-
- [1] K. B. Rundman and J. E. Hilliard, Early stages of spinodal decomposition in an aluminum-zinc alloy, *Acta. Metall.* **15**, 1025 (1967).
 - [2] A. J. Ardell and R. B. Nicholson, The coarsening of γ' in Ni-Al alloys, *J. Phys. Chem. Solids* **27**, 1793 (1966).
 - [3] S. Katano and M. Iizumi, Crossover Phenomenon in Dynamical Scaling of Phase Separation in Fe-Cr Alloy, *Phys. Rev. Lett.* **52**, 835 (1984).
 - [4] B. D. Gaulin, S. Spooner, and Y. Morii, Kinetics of Phase Separation in $\text{Mn}_{0.67}\text{Cu}_{0.33}$, *Phys. Rev. Lett.* **59**, 668 (1987).
 - [5] J. J. Hoyt, B. Clark, D. de Fontaine, J. P. Simon, and O. Lyon, A synchrotron radiation study of phase separation in AlZn alloys-I. Kinetics, *Acta. Metall.* **37**, 1597 (1989).
 - [6] F. S. Bates and P. Wilzius, Spinodal decomposition of a symmetric critical mixture of deuterated and protonated polymer, *J. Chem. Phys.* **91**, 3258 (1989).
 - [7] O. Krichevsky and J. Stavans, Correlated Ostwald Ripening in Two Dimensions, *Phys. Rev. Lett.* **70**, 1473 (1993).
 - [8] M. Seul, N. Y. Morgan, and C. Sire, Domain Coarsening in a Two-Dimensional Binary Mixture: Growth Dynamics and Spatial Correlations, *Phys. Rev. Lett.* **73**, 2284 (1994).
 - [9] I. Seyhan, L. Ratke, W. Bender, and P. W. Voorhees, Ostwald ripening of solid-liquid Pb-Sn dispersions, *Metall. Mater. Trans. A* **27**, 2470 (1995).
 - [10] J. Mainville, Y. S. Yang, K. R. Elder, M. Sutton, K. F. Ludwig, and G. B. Stephenson, X-Ray Scattering Study of Early Stage Spinodal Decomposition in $\text{Al}_{0.62}\text{Zn}_{0.38}$, *Phys. Rev. Lett.* **78**, 2787 (1997).
 - [11] J. Alkemper, V. A. Snyder, N. Akaiwa, and P. W. Voorhees, Dynamics of Late-Stage Phase Separation: A Test of Theory, *Phys. Rev. Lett.* **82**, 2725 (1999).
 - [12] V. A. Snyder, J. Alkemper, and P. W. Voorhees, The development of spatial correlations during Ostwald ripening: A test of theory, *Acta Mater.* **48**, 2689 (2000).
 - [13] N. C. Lautze, T. W. Sisson, M. T. Margaret, and T. L. Grove, Segregating gas from melt: An experimental study of the Ostwald ripening of vapor bubbles in magmas, *Contrib. Mineral. Petrol.* **161**, 331 (2011).
 - [14] J. W. Cahn and J. E. Hilliard, Free energy of a nonuniform system. III. Nucleation in a two-component incompressible fluid, *J. Chem. Phys.* **31**, 688 (1959).
 - [15] I. M. Lifshitz and V. V. Slyozov, The kinetics of precipitation from supersaturated solid solutions, *J. Phys. Chem. Solids* **19**, 35 (1961).
 - [16] C. Wagner, Theorie der Alterung von Niederschlagen durch Umlosen (Ostwald reifung), *Z. Elektrochem.* **65**, 581 (1961).
 - [17] H. E. Cook, Brownian motion in spinodal decomposition, *Acta. Metall.* **18**, 297 (1970).
 - [18] J. S. Langer, M. Bar-on, and H. Miller, New computational method in the theory of spinodal decomposition, *Phys. Rev. A* **11**, 1417 (1975).
 - [19] E. D. Siggia, Late stages of spinodal decomposition in binary mixtures, *Phys. Rev. A* **20**, 595 (1979).
 - [20] J. A. Marqusee and J. Ross, Theory of Ostwald ripening: Competitive growth and its dependence on volume fraction, *J. Chem. Phys.* **80**, 536 (1984).
 - [21] P. W. Voorhees, The theory of Ostwald ripening, *J. Stat. Phys.* **38**, 231 (1985).
 - [22] M. Marder, Correlations and Droplet Growth, *Phys. Rev. Lett.* **55**, 2953 (1985).
 - [23] A. J. Ardell, Late-stage two-dimensional coarsening of circular clusters, *Phys. Rev. B* **41**, 2554 (1990).
 - [24] J. H. Yao, K. R. Elder, H. Guo, and M. Grant, Theory and simulation of Ostwald ripening, *Phys. Rev. B* **47**, 14110 (1993).
 - [25] N. Akaiwa and P. W. Voorhees, Late-stage phase separation: Dynamics, spatial correlations, and structure functions, *Phys. Rev. E* **49**, 3860 (1994).
 - [26] F. Haußer and A. Voigt, Ostwald ripening in two-dimensional homoepitaxial islands, *Phys. Rev. B* **72**, 035437 (2005).
 - [27] C. Roland and M. Grant, Monte Carlo Renormalization-Group Study of the Late-Stage Dynamics of Spinodal Decomposition, *Phys. Rev. Lett.* **60**, 2657 (1988).
 - [28] T. M. Rogers, K. R. Elder, and R. C. Desai, Numerical study of the late stages of spinodal decomposition, *Phys. Rev. B* **37**, 9638 (1988).

- [29] M. Laradji, M. Grant, M. J. Zuckermann, and W. Klein, Dynamics of first-order transitions in two-dimensional systems with long-range interactions, *Phys. Rev. B* **41**, 4646 (1990).
- [30] N. Masbaum, Simulation of Ostwald ripening in two dimensions: Spatial and nearest neighbor correlations, *J. Phys. I* **5**, 1143 (1995).
- [31] M. Laradji, S. Toxvaerd, and O. G. Mouritsen, Molecular Dynamics Simulation of Spinodal Decomposition in Three-Dimensional Binary Fluids, *Phys. Rev. Lett.* **77**, 2253 (1996).
- [32] T. Lookman, Y. Wu, F. J. Alexander, and S. Chen, Spinodal decomposition in fluids: Diffusive, viscous, and inertial regimes, *Phys. Rev. E* **53**, 5513 (1996).
- [33] B. F. Barton, P. D. Graham, and A. J. McHugh, The Dynamics of thermal-induced phase separation in PMMA solutions, *Macromolecules (Washington, DC, U. S.)* **31**, 1672 (1998).
- [34] J. Midya and S. K. Das, Kinetics of Vapor-Solid Phase Transitions: Structure, Growth, and Mechanism, *Phys. Rev. Lett.* **118**, 165701 (2017).
- [35] A. J. Bray, Theory of phase-ordering kinetics, *Adv. Phys.* **43**, 357 (1994).
- [36] J. D. Gunton, M. San Miguel, and P. S. Sahni, in *Phase Transitions and Critical Phenomena*, edited by C. Domb and J. L. Lebowitz (Academic Press, New York, 1983), Vol. 8, p. 265.
- [37] J. Svoboda and F. D. Fisher, Generalization of the Lifshitz-Slyozov-Wagner coarsening theory to non-dilute multi-component systems, *Acta Mater.* **79**, 304 (2014).
- [38] R. O. Jones, Density functional theory: Its origins, rise to prominence, and future, *Rev. Mod. Phys.* **87**, 897 (2015).
- [39] M. I. Baskes, Modified embedded-atom potentials for cubic materials and impurities, *Phys. Rev. B* **46**, 2727 (1992).
- [40] S. A. Etesami, M. I. Baskes, M. Laradji, and E. Asadi, Thermodynamics of solid Sn and Pb-Sn liquid mixtures using molecular dynamics simulations, *Acta Mater.* **161**, 320 (2018).
- [41] I. Steinbach, Phase-field models in materials science, *Modell. Simul. Mater. Sci. Eng.* **17**, 073001 (2009).
- [42] K. R. Elder and M. Grant, Modeling elastic and plastic deformations in nonequilibrium processing using phase field crystals, *Phys. Rev. E* **70**, 051605 (2004).
- [43] Z.-F. Huang and K. R. Elder, Mesoscopic and Microscopic Modeling of Island Formation in Strained Film Epitaxy, *Phys. Rev. Lett.* **101**, 158701 (2008).
- [44] K.-A. Wu and P. W. Voorhees, Stress-induced morphological instabilities at the nanoscale examined using the phase field crystal approach, *Phys. Rev. B* **80**, 125408 (2009).
- [45] K. R. Elder, N. Provatas, J. Berry, P. Stefanovic, and M. Grant, Phase-field crystal modeling and classical density functional theory of freezing, *Phys. Rev. B* **75**, 064107 (2007).
- [46] S. van Teeffelen, R. Backofen, A. Voigt, and H. Löwen, Derivation of the phase-field-crystal model for colloidal solidification, *Phys. Rev. E* **79**, 051404 (2009).
- [47] G. Tegze, L. Gránásy, G. I. Tóth, F. Podmaniczky, A. Jaatinen, T. Ala-Nissila, and T. Pusztai, Diffusion-Controlled Anisotropic Growth of Stable and Metastable Crystal Polymorphs in the Phase-Field Crystal Model, *Phys. Rev. Lett.* **103**, 035702 (2009).
- [48] N. Ofori-Opoku, V. Fallah, M. Greenwood, S. Esmaeili, and N. Provatas, Multicomponent phase-field crystal model for structural transformations in metal alloys, *Phys. Rev. B* **87**, 134105 (2013).
- [49] A. Cartalade, A. Younsi, É. Régnier, and S. Schuller, Simulations of Phase-field Models for Crystal Growth and Phase Separation, *Proc. Mat. Sci.* **7**, 72 (2014).
- [50] Y. Tao, C. Zheng, Z. Jing, D. Weiping, and W. Lin, Phase field crystal study on the temporal evolution and coarsening mechanism of precipitates during spinodal decomposition, *Rare Met. Mater. Eng.* **42**, 1773 (2013).
- [51] E. M. Wong, J. E. Bonevich, and P. C. Searson, Growth kinetics of nanocrystalline ZnO particles from colloidal suspensions, *J. Phys. Chem. B* **102**, 7770 (1998).
- [52] G. Oskam, A. Nellore, R. L. Penn, and P. C. Searson, The growth kinetics of TiO₂ nanoparticles from titanium(IV) alkoxide at high water/titanium ratio, *J. Phys. Chem. B* **107**, 1734 (2003).
- [53] M. Marder, Correlations and Ostwald ripening, *Phys. Rev. A* **36**, 858 (1987).
- [54] T. M. Rogers and R. C. Desai, Numerical study of late-stage coarsening for off-critical quenches in the Cahn-Hilliard equation of phase separation, *Phys. Rev. B* **39**, 11956 (1989).
- [55] S. N. Chiu, Aboav-Weaire and Lewis' laws—A review, *Mater. Charact.* **34**, 149 (1995).
- [56] N. Provatas and K. R. Elder, *Phase-Field Methods in Materials Science and Engineering* (Wiley-VCH, Weinheim, 2010).
- [57] S. K. Sinha, E. B. Sirota, S. Garoff, and H. B. Stanley, X-ray and neutron scattering from rough surfaces, *Phys. Rev. B* **38**, 2297 (1988).
- [58] J. Duplat, B. Bossa, and E. Villermaux, *On Two-Dimensional Foam Ageing*, *J. Fluid Mech.* **673**, 147 (2011).
- [59] N. F. Rivier, G. Schliecker, and B. Dubertret, The stationary state of epithelia, *Acta Biotheor.* **43**, 403 (1995).
- [60] F. Glassmeier and G. Feingold, Network approach to patterns in stratocumulus clouds, *Proc. Natl. Acad. Sci. USA* **114**, 10578 (2017).
- [61] H. Flyvbjerg, Model for coarsening froths and foams, *Phys. Rev. E* **47**, 4037 (1993).
- [62] C. Sire and M. Seul, Maximum entropy analysis of disordered droplet patterns, *J. Phys. I* **5**, 97 (1995).
- [63] A. Jaatinen, C. V. Achim, K. R. Elder, and T. Ala-Nissila, Thermodynamics of bcc metals in phase-field crystal models, *Phys. Rev. E* **80**, 031602 (2009).
- [64] E. Asadi and M. Asle Zaem, S. Nouranian, and M. I. Baskes, Quantitative modeling of the equilibration of two-phase solid-liquid Fe by atomistic simulations on diffusive time scales, *Phys. Rev. B* **91**, 024105 (2015).